An unsteady aerodynamic/aeroacoustic optimization framework using continuous adjoint

M. Monfaredi, X. S. Trompoukis, K. T. Tsiakas and K.C. Giannakoglou

Abstract In this paper, an unsteady aerodynamic/aeroacoustic optimization framework is presented. This is based on the continuous adjoint method to a hybrid acoustic prediction tool, in which the near-field flow solution results from an unsteady CFD simulation while the acoustic propagation to far-field makes use of an acoustic analogy. The CFD simulation is performed using the in-house GPU-enabled URANS equations' solver for which a continuous adjoint solver is available. The noise prediction tool and its adjoint are developed based on the permeable version of the Ffowcs Williams and Hawkings (FW-H) analogy, solved in the frequency domain. Its implementation is verified w.r.t. the analytical solution of the sound field from a monopole source in uniform flow. Then, the accuracy of the hybrid solver is verified by comparing the sound directivity computed by the FW-H analogy with that of a CFD run, for a 2D pitching airfoil in a subsonic inviscid flow. The accuracy of the sensitivities computed using the unsteady adjoint solver is verified w.r.t. those computed by finite differences. Finally, the programmed software is used to optimize the shape of the pitching airfoil, aiming at min. noise with an equality constraint for the lift.

1 Introduction

During the last decades, there have been tight regulations regarding noise pollution which underline the importance of an effective noise source mitigation strategy. For example, based on the Flightpath 2050 report of the European Commission [1], it is

M. Monfaredi, e-mail: morteza.monfaredi@gmail.com
X. S. Trompoukis, e-mail: xeftro@gmail.com
K. T. Tsiakas, e-mail: tsiakost@gmail.com
K.C. Giannakoglou, e-mail: kgianna@central.ntua.gr
Parallel CFD & Optimization Unit, School of Mechanical Engineering, National Technical University of Athens (NTUA), Athens, Greece.

mandated to reduce the perceived noise by 65% from its level in 2000, by the year 2050. This means designers must investigate innovative methods to further improve the process of designing quieter and more efficient systems. Among the various existing methods performing numerical optimization, adjoint methods [2, 3], are advantageous since their computational cost is independent of the number of design variables.

Although adjoint methods have a strong background in aerodynamic shape optimization [4], they are relatively new in the field of aeroacoustic optimization [5, 6, 7, 8, 9, 10, 11, 12]. In [5], a steady continuous adjoint method was presented for the reduction of the noise perceived by the car driver due to its side mirror using a turbulence-based surrogate objective function. With this model, the omission of the adjoint to the turbulence model equations would merely lead to zero sensitivities, since the objective depends only on turbulence. In [6], a discrete adjoint to a hybrid URANS-FW-H solver was developed for inverse shape design and turbulent blunt trailing edge noise reduction. Recently, the same method has been used to perform shape optimization to reduce the far-field noise from a pitching airfoil in an inviscid flow [7], a 2D wing-flap in laminar flow [8], a rod-airfoil in turbulent flow [9] and a jet-flap interaction in turbulent flow [10]. In these works [6, 7, 8, 9, 10], discrete adjoint was used with the help of automatic differentiation. Regarding continuous adjoint, the permeable FW-H formula is solved using a finite element method, leading to the necessary adjoint conditions at the interface between the Computational Fluid Dynamics (CFD) and Computational Aeroacoustics (CAA) domains [11]. The continuous adjoint for a hybrid solver for incompressible flow models and the Kirchhoff integral, for automotive applications, can also be found in the literature [12]. To the author's knowledge, the continuous adjoint method to compressible flows based on the FW-H analogy appears, for the first time, in this paper.

For the first verification of the method presented in this paper, the CFD model is restricted to the Euler equations. A hybrid aeroacoustic noise prediction tool is built on the in-house GPU-enabled flow solver [13, 14], by additionally implementing the FW-H analogy. For its verification, numerical results are compared with the analytical solution of a monopole sound source in a flow-stream, and CFD results for a 2D pitching isolated airfoil. Then, the continuous adjoint method is verified and used to perform shape optimization, with an aeroacoustic objective function and an aerodynamic equality constraint.

2 Governing Equations

2.1 Flow Equations

The 2D unsteady inviscid flow equations of a compressible fluid are discretized using a dual-time stepping method, being second-order accurate in time. Spatial discretization is based on vertex-centered finite volume. Convective fluxes are computed using

the upwind Roe scheme, with second-order accuracy in space. The discretization of the governing equations in the pitching airfoil case takes the geometrical conservation law into account. Along the far-field boundary, a non-reflecting condition is applied [15].

2.2 Noise prediction using the FW-H analogy

Based on the assumption that sound is perceived as pressure fluctuations, acoustic noise can be computed using CFD simulations. However, a purely CFD-based approach may become very expensive when the acoustic noise at a far-field location is of interest, because the fine CFD mesh should be extended far away, up to the receiver's location. The combination of CFD methods and acoustic analogies rely upon the computationally cheaper wave equation. Such methods are usually referred to as hybrid methods and their origin can be traced back to the Lighthill analogy [16] ; this was later extended by Curle [17] to account for the presence of stationary solid surface and Ffowcs Williams and Hawkings to include moving surfaces [18]. In this paper, the permeable version of FW-H analogy is used. The resulting wave equation, a.k.a. the FW-H equation, reads:

$$\frac{\partial^2}{\partial t^2} \quad c_1^2 \frac{\partial^2}{\partial x_i \partial x_i} \quad {}^1H^1 f^0 p^{\prime 0} = \frac{\partial}{\partial t} {}^1Q\delta^1 f^{00} \quad \frac{\partial}{\partial x_i} {}^1F_i \delta^1 f^{00} + \frac{\partial^2}{\partial x_i \partial x_j} {}^1H^1 f^0 T_{ij}{}^0 \quad (1)$$

and for bodies in motion (such as a pitching airfoil in uniform flow), the Galilean transformation can be used to transform Eq. 1 into a relative system associated with the moving body, as follows [19] :

$$\begin{aligned} &\frac{\partial^2}{\partial t^2} + v_{1\,i} v_{1\,j} \frac{\partial^2}{\partial x_i \partial x_j} + 2 v_{1\,i} \frac{\partial^2}{\partial x_i \partial t} \quad c_1^2 \frac{\partial^2}{\partial x_i \partial x_i} \quad {}^1H^1 f^0 p^{\prime 0} \\ &\quad = \frac{\partial}{\partial t} {}^1Q\delta^1 f^{00} \quad \frac{\partial}{\partial x_i} {}^1F_i \delta^1 f^{00} + \frac{\partial^2}{\partial x_i \partial x_j} {}^1H^1 f^0 T_{ij}{}^0 \end{aligned} \quad (2)$$

where f is the signed distance from the interface of the CFD and CAA domains, as shown in fig.1. This interface will be referred to as the FW-H surface. The FW-H surface lays inside the CFD domain though far away from the body in order for this not to be affected by changes in the body shape to be designed. H is the Heaviside function, δ is the Dirac delta function and c_1 is the free-stream sound speed. ${}^1Q\vec{x}, t^0 = {}^1\rho v_i \quad \rho_1 v_{1\,i}{}^0 n_i$, ${}^1F_i\vec{x}, t^0 = {}^1\rho^1 v_i \quad 2 v_{1\,i}{}^0 + \rho_1 v_{1\,i} v_{1\,j} + p\delta_{ij} \quad \tau_{ij}{}^0 n_j$ and ${}^1T_{ij}\vec{x}, t^0 = \rho^1 v_i \quad v_{1\,i}{}^{01} v_j \quad v_{1\,j}{}^0 + {}^1p \quad c_1^2 \rho^0 \delta_{ij}$ are known as the monopole, dipole and quadrupole source terms, respectively, defined along the FW-H surface. $\rho = \rho_1 + \rho^0$, $p = p_1 + p^0$ and $v_i = v_{1\,i} + v_i^0$ are local density, pressure and velocity components, respectively, and τ_{ij} is the viscous stress tensor. Free-stream quantities are indexed by 1. $\vec{n}$ is the unit normal vector to the FW-H surface pointing towards the CAA domain. δ_{ij} is the Kronecker delta.

For 3D problems, integral solutions to the FW-H equation are available in the time domain. However, in 2D problems, to avoid tail effects, an infinitely long time integration range must be used. To avoid this, Eq. 2 is transformed into the frequency domain using the Fourier transformation as follows:

$$\frac{\partial^2}{\partial x_i \partial x_i} + k^2 \quad 2iM_{1\,i}k\frac{\partial}{\partial x_i} \quad M_{1\,i}M_{1\,j}\frac{\partial^2}{\partial x_i \partial x_j} \quad {}^1H^1f^0\hat{p}^{00} = i\omega\hat{Q}\delta^1f^0 + \frac{\partial}{\partial x_i}{}^1\hat{F}_i\delta^1f^{00} \quad \frac{\partial^2}{\partial x_i \partial x_j}{}^1H^1f^0\hat{T}_{ij}{}^0 \tag{3}$$

where the hat symbol (ˆ) denotes frequency domain variables and ω is the frequency. $M_{1\,i} = v_{1\,i} \bullet c_1$ and the wave number is $k = \omega \bullet c_1$. Eq. 3 is solved by convolving it with the appropriate Green function. Then, the pressure fluctuation in the frequency domain, at the receiver's location, results from:

$$H^1f^0\hat{p}^{01}\vec{x}_o, \omega^0 = \int_{f=0}^{2} i\omega\hat{Q}^1\vec{x}_s, \omega^0\hat{G}^1\vec{x}_o, \vec{x}_s, \omega^0 ds \int_{f=0}^{2} \hat{F}_i{}^1\vec{x}_s, \omega^0 \frac{\partial\hat{G}^1\vec{x}_o, \vec{x}_s, \omega^0}{\partial x_{s\,i}} ds \int_{f>0}^{2} \hat{T}_{ij}{}^1\vec{x}_s, \omega^0 \frac{\partial^2\hat{G}^1\vec{x}_o, \vec{x}_s, \omega^0}{\partial x_{s\,i}\partial x_{s\,j}} dV \tag{4}$$

where $\vec{x}_o$ and $\vec{x}_s$ are the receiver and sources' (sources are located on the FW-H surface) positions, respectively. $\hat{G}^1\vec{x}_o, \vec{x}_s, \omega^0$ is the 2D Green function for subsonic flows in the frequency domain, which is defined as:

$$\hat{G}^1\vec{x}_o, \vec{x}_s, \omega^0 = \frac{i}{4\beta}\exp^1 iM_1 k\bar{x}_1 \bullet \beta^{2\,0}H_0^{12^0} \quad \frac{k}{\beta^2} \quad \sqrt{\bar{x}_1^2 + \beta^2\bar{x}_2^2} \tag{5}$$

$$\bar{x}_1 = {}^1x_{o1} \quad x_{s1}{}^0\cos\theta + {}^1x_{o2} \quad x_{s2}{}^0\sin\theta \tag{6}$$

$$\bar{x}_2 = {}^1x_{o1} \quad x_{s1}{}^0\sin\theta + {}^1x_{o2} \quad x_{s2}{}^0\cos\theta \tag{7}$$

In the above equations, θ is the free-stream flow angle, such that $\tan\theta = \frac{v_{1\,2} \bullet v_{1\,1}}{}$, M_1 is the free-stream Mach number and the Prandtl-Glauert factor is $\beta = \sqrt{1 \quad M_1^2}$. $H_0^{12^0}$ stands for Hankel function of the second kind of zero order.

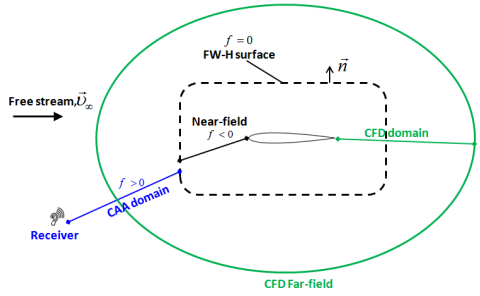

Fig. 1 Schematic of permeable FW-H surface. The dashed-line shows the interface between the CFD and CAA domains.

For the low-speed cases this paper is dealing with, the contribution of quadrupole terms can be neglected, avoiding thus the computation of a volume integral. The noise prediction module is combined with the in-house flow solver as follows: first, an unsteady flow solution is performed in the CFD domain and, at the end of each time step, source terms Q and F_i are computed over the FW-H surface. Upon completion of the unsteady CFD simulation, the mean value of each source is subtracted from instantaneous values since the mean value corresponds to zero frequency that does not generate noise. Since it is hard to achieve pure periodic results, a Hanning window is applied to the sources to eliminate discontinuity between the first and last points, followed by a Fourier transform. At the end, pressure fluctuations in the frequency domain are computed using Eq. 4.

3 Formulation of the continuous adjoint method

In aerodynamic shape optimization, adjoint methods compute the gradient of an objective function w.r.t. the design variables. The objective functions, such as the lift, drag etc. are integral quantities defined along the solid boundaries and contribute to either the adjoint boundary conditions or the adjoint sensitivities. On the other hand, in aeroacoustic problems, the objective function is defined at the remote receiver's location, $\vec{x}_o$, and affects neither the adjoint boundary conditions nor the sensitivities; instead this contributes to the adjoint equations in the form of source terms applied along the FW-H surface. An objective function J, originally written as a time integral of p', can also be expressed in the frequency domain as:

$$J = \int_{\omega} |\hat{p}'(\vec{x}_o, \omega)| d\omega \tag{8}$$

where $\hat{p}'(\vec{x}_o, \omega)$ is the outcome of Eq. 4 and $|\hat{p}'| = \sqrt{\hat{p}'^2_{Re} + \hat{p}'^2_{Im}}$, where subscripts Re and Im refer to the real and imaginary parts of complex variables. Here, the integration range is over the whole frequency domain.

To formulate the continuous adjoint problem, an augmented objective function is defined as $F_{aug} = J + \int_T \int \psi_n R_n d\Omega dt$, where $n = 1, 4$ and ψ_n, R_n, Ω and T are the adjoint variable fields, the residuals of the unsteady Euler equations, the CFD domain and the solution period, respectively. By differentiating F_{aug} w.r.t. the design variables b_n and setting the multipliers of the variations in the flow variables to zero, the unsteady adjoint equations are obtained as:

$$\frac{\partial \psi_m}{\partial t} \int_{\Omega} A_{nmk} \frac{\partial \psi_n}{\partial x_k} + \int_{S_{FW}} H_m \delta' f' = 0 \tag{9}$$

where $A_{nmk} = \frac{\delta g_{nk}}{\delta U_m}$. U_m and g_{nk} are the conservative flow variables and inviscid fluxes, respectively. The adjoint boundary condition along the solid walls is

$\psi_{m+1} n_{w_m} + {}^1u_m^{grid} n_{w_m} {}^o\psi_4 = 0$, where $\vec{n}_w$ is the unit normal to the wall and u_m^{grid} is the grid velocity at each node on the pitching airfoil. b_n are the coordinates of the control points of the shape parameterization method which is based on Bezier polynomials.

In Eq. 9, $S_{FW\_H_m}$ is a term that includes contributions from the FW-H analogy to the adjoint equations. To find this term, Eq. 8 is differentiated w.r.t. b_n, as follows:

$$\frac{\delta J}{\delta b_n} = \int_\omega \frac{1}{|\hat{p}^0|} \hat{p}^0{}_{\mathrm{Re}} \frac{\delta \hat{p}^0{}_{\mathrm{Re}}}{\delta b_n} \, d\omega + \int_\omega \frac{1}{|\hat{p}^0|} \hat{p}^0{}_{\mathrm{Im}} \frac{\delta \hat{p}^0{}_{\mathrm{Im}}}{\delta b_n} \, d\omega \tag{10}$$

For the sake of simplicity, starting from Eq. 10, $\hat{p}^0{}^1\vec{x}_o, \omega^o$, $\hat{G}^1\vec{x}_o, \vec{x}_s, \omega^o$, $\hat{F}_k{}^1\vec{x}_s, \omega^o$ and $\hat{Q}^1\vec{x}_s, \omega^o$ are shorted to $\hat{p}^0$, $\hat{G}$, $\hat{F}_k$ and $\hat{Q}$, respectively. The real and imaginary part of the $\hat{p}^0$ can be found based on Eq. 4. Since the grid does not change at the FW-H surface location during the optimization, the derivatives of the Green function and its spatial derivatives as well as those of the surface element ds, w.r.t. b_n are zero. So, the variation of the real and imaginary part of $\hat{p}^0$ w.r.t. b_n read:

$$\begin{aligned} \frac{\delta \hat{p}^0_{\mathrm{Re}}}{\delta b_n} = & \int_{f=0}^{2} \Big[\frac{\delta \hat{F}_k}{\delta b_n}_{\mathrm{Re}} \frac{\delta \hat{G}}{\delta x_{s_k}}_{\mathrm{Re}} - \frac{\delta \hat{F}_k}{\delta b_n}_{\mathrm{Im}} \frac{\delta \hat{G}}{\delta x_{s_k}}_{\mathrm{Im}} \Big] ds \\ & + \int_{f=0}^{2} \omega \Big[\frac{\delta \hat{Q}}{\delta b_n}_{\mathrm{Re}} \hat{G}_{\mathrm{Im}} + \frac{\delta \hat{Q}}{\delta b_n}_{\mathrm{Im}} \hat{G}_{\mathrm{Re}} \Big] ds \end{aligned} \tag{11}$$

and

$$\begin{aligned} \frac{\delta \hat{p}^0_{\mathrm{Im}}}{\delta b_n} = & \int_{f=0}^{2} \Big[\frac{\delta \hat{F}_k}{\delta b_n}_{\mathrm{Re}} \frac{\delta \hat{G}}{\delta x_{s_k}}_{\mathrm{Im}} + \frac{\delta \hat{F}_k}{\delta b_n}_{\mathrm{Im}} \frac{\delta \hat{G}}{\delta x_{s_k}}_{\mathrm{Re}} \Big] ds \\ & - \int_{f=0}^{2} \omega \Big[\frac{\delta \hat{Q}}{\delta b_n}_{\mathrm{Re}} \hat{G}_{\mathrm{Re}} - \frac{\delta \hat{Q}}{\delta b_n}_{\mathrm{Im}} \hat{G}_{\mathrm{Im}} \Big] ds \end{aligned} \tag{12}$$

By introducing Eqs. 11 and 12 in Eq. 10, the derivatives of J become:

$$\begin{aligned} \frac{\delta J}{\delta b_n} = & - \int_\omega \int_{f=0}^{2} \Big[\frac{1}{|\hat{p}^0|} \Big(\hat{p}^0_{\mathrm{Re}} \frac{\delta \hat{G}}{\delta x_{s_k}}_{\mathrm{Re}} + \hat{p}^0_{\mathrm{Im}} \frac{\delta \hat{G}}{\delta x_{s_k}}_{\mathrm{Im}} \Big) \frac{\delta \hat{F}_k}{\delta b_n}_{\mathrm{Re}} \Big] ds d\omega \\ & - \int_\omega \int_{f=0}^{2} \Big[\frac{1}{|\hat{p}^0|} \Big(\hat{p}^0_{\mathrm{Im}} \frac{\delta \hat{G}}{\delta x_{s_k}}_{\mathrm{Re}} - \hat{p}^0_{\mathrm{Re}} \frac{\delta \hat{G}}{\delta x_{s_k}}_{\mathrm{Im}} \Big) \frac{\delta \hat{F}_k}{\delta b_n}_{\mathrm{Im}} \Big] ds d\omega \\ & - \int_\omega \int_{f=0}^{2} \omega \frac{1}{|\hat{p}^0|} \Big(\hat{p}^0_{\mathrm{Re}} \hat{G}_{\mathrm{Im}} + \hat{p}^0_{\mathrm{Im}} \hat{G}_{\mathrm{Re}} \Big) \frac{\delta \hat{Q}}{\delta b_n}_{\mathrm{Re}} ds d\omega \\ & + \int_\omega \int_{f=0}^{2} \omega \frac{1}{|\hat{p}^0|} \Big(\hat{p}^0_{\mathrm{Re}} \hat{G}_{\mathrm{Re}} - \hat{p}^0_{\mathrm{Im}} \hat{G}_{\mathrm{Im}} \Big) \frac{\delta \hat{Q}}{\delta b_n}_{\mathrm{Im}} ds d\omega \end{aligned} \tag{13}$$

In Eq. 13, $\frac{\delta \hat{F}_k}{\delta b_n}$ and $\frac{\delta \hat{Q}}{\delta b_n}$ include derivatives of the flow variables w.r.t. the design variables in the frequency domain. However, these variations should be expressed in the time domain for them to contribute to the adjoint flow equations. To do so, the Fourier transformation needs to be included in Eq. 13, by considering the subtraction

of the time-averaged value of F_k and Q from their instantaneous values, along with a multiplication with the Hanning window $H(t)$ before transforming them into the frequency domain. Hence, the Fourier transformation for an arbitrary signal $s(t)$ is performed as follows:

$$\hat{s}(\omega) = \frac{1}{T}\int_T H(t)\, s(t) \left[\frac{1}{T}\int_T s(t)dt\, e^{-2i\pi\omega t}\right] dt \tag{14}$$

Including Eq. 14 into Eq. 13 and permuting time and frequency integrals, $\frac{\delta J}{\delta b_n}$ reads:

$$\frac{\delta J}{\delta b_n} = \frac{1}{T}\int_{T}\int_{f=0}^{-} 2\left[A_k + B_k \frac{\delta F_k}{\delta b_n} + C + D\frac{\delta Q}{\delta b_n}\right] ds dt \tag{15}$$

where

$$A_k = \int_{\omega}^{-} \left[\frac{\hat{p}'_{\mathrm{Re}}}{|\hat{p}'|}\left(\frac{\partial \hat{G}}{\partial x_{s_k}}\right)_{\mathrm{Re}} + \frac{\hat{p}'_{\mathrm{Im}}}{|\hat{p}'|}\left(\frac{\partial \hat{G}}{\partial x_{s_k}}\right)_{\mathrm{Im}}\right] H(t)\cos(2\pi\omega t)\, H_c(\omega) d\omega \tag{16}$$

$$B_k = \int_{\omega}^{-} \left[\frac{\hat{p}'_{\mathrm{Re}}}{|\hat{p}'|}\left(\frac{\partial \hat{G}}{\partial x_{s_k}}\right)_{\mathrm{Im}} + \frac{\hat{p}'_{\mathrm{Im}}}{|\hat{p}'|}\left(\frac{\partial \hat{G}}{\partial x_{s_k}}\right)_{\mathrm{Re}}\right] H(t)\sin(2\pi\omega t)\, H_s(\omega) d\omega \tag{17}$$

$$C = \int_{\omega}^{-} \left[\frac{\hat{p}'_{\mathrm{Im}}}{|\hat{p}'|}\hat{G}_{\mathrm{Re}} - \frac{\hat{p}'_{\mathrm{Re}}}{|\hat{p}'|}\hat{G}_{\mathrm{Im}}\right] H(t)\cos(2\pi\omega t)\, H_c(\omega) d\omega \tag{18}$$

$$D = \int_{\omega}^{-} \left[\frac{\hat{p}'_{\mathrm{Im}}}{|\hat{p}'|}\hat{G}_{\mathrm{Im}} - \frac{\hat{p}'_{\mathrm{Re}}}{|\hat{p}'|}\hat{G}_{\mathrm{Re}}\right] H(t)\sin(2\pi\omega t)\, H_s(\omega) d\omega \tag{19}$$

$$H_c(\omega) = \frac{1}{T}\int_{T}^{-} H(t)\cos(2\pi\omega t) dt \tag{20}$$

$$H_s(\omega) = \frac{1}{T}\int_{T} H(t)\sin(2\pi\omega t) dt \tag{21}$$

Equation 15 contains a double time/surface integral over the FW-H surface. Therefore, in order to eliminate the derivatives of the flow variables w.r.t. b_n, this equation is taken into account as source terms (S_{FW_Hm} in Eq. 9) at the cells lying along the FW-H surface, when solving the adjoint equations. Since the in-house code solves for the conservative variables, F_k and Q must be expressed in terms of these variables before differentiation, yielding:

$$\frac{\delta F_k}{\delta b_n} = \delta_{kj}(\gamma - 1)\left[\frac{|\vec{v}|^2}{2}\frac{\delta U_1}{\delta b_n} - v_j\left(\frac{\delta U_{j+1}}{\delta b_n} + \frac{\delta U_4}{\delta b_n}\right)n_j\right] + v_k\left[2v_{1k}\left(\frac{\delta U_{j+1}}{\delta b_n}n_j\right) + v_j n_j\frac{\delta U_{k+1}}{\delta b_n} - v_j n_j v_k\frac{\delta U_1}{\delta b_n}\right] \tag{22}$$

$$\frac{\delta Q}{\delta b_n} = n_k\frac{\delta U_{k+1}}{\delta b_n} \tag{23}$$

where $k = 1, 2$ and $j = 1, 2$ are the Cartesian directions; γ is the heat capacity ratio. Since the FW-H surface remains invariant during the optimization, for the FW-H surface nodes, total and partial derivatives of flow variable are identical or

$\frac{\delta}{\delta b_n} = \frac{\partial}{\partial b_n}$. Using Eqs. 22 and 23 in Eq. 15, replacing total with partial derivatives and canceling all derivatives of the flow variables w.r.t. b_n, the $S_{FW\_H_m}$ term reads:

$$S_{FW\_H} = \begin{bmatrix} \frac{1}{2}\left(\gamma - 1\right)\left|v\right|^2 n_k & -v_i n_i v_k & A_k + B_k \\ \left(\gamma v_1 n_k + v_k\right) & \left(2v_{1k} n_1 - g\right) & A_k + B_k + v_i n_i A_1 + B_1 + n_1 C + D \\ \left(\gamma v_2 n_k + v_k\right) & \left(2v_{1k} n_2 - g\right) & A_k + B_k + v_i n_i A_2 + B_2 + n_2 C + D \\ \gamma - 1 & n_k & A_k + B_k \end{bmatrix} \quad (24)$$

and the J sensitivities are computed as follows:

$$\frac{\delta J}{\delta b_n} = \int_T \psi_i \frac{\partial U_i}{\partial x_k}\frac{\partial}{\partial t}\left(\frac{\delta x_k}{\delta b_n}\right) d\,dt - \int_T \psi_i \frac{\partial g_{ik}}{\partial x_e}\frac{\partial}{\partial x_k}\left(\frac{\delta x_e}{\delta b_n}\right) d\,dt - \int_{T\,s} \psi_i g_{ik}\frac{\delta n_k}{\delta b_n}\,ds\,dt \quad (25)$$

where s is the solid wall which in this case is the airfoil surface.

A single cycle of the CFD-CAA optimization framework is shown in fig. 2.

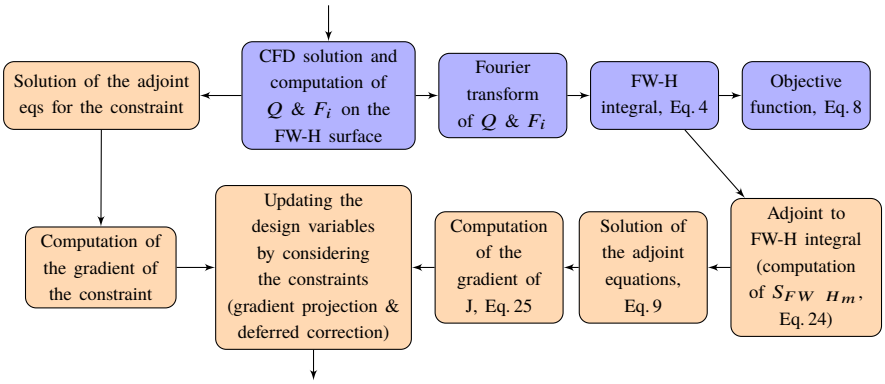

Fig. 2 A single cycle of the CFD-CAA Optimization. Primal and adjoint workflow in blue and orange, respectively.

3.1 Constraint imposition methods

In the constrained case, a gradient projection method with an additional correction term is used to impose an equality constraint on the lift force. Although gradient projection methods are very effective when the constraint function is linear w.r.t. b_n, they lack efficiency otherwise. In case of a non-linear constraint, the optimization is not able to follow the constraint line and gradually deviates from it. To overcome this, the standard gradient projection method is enhanced with a deferred correction.

Let J be the objective function to be minimized subjected to the constraint $L = L_1$. The design variables $\vec{b}$ are updated using a constant step η. Instead of updating each design variable by adding

$$\delta\vec{b}_{projected} = \eta \left[\vec{\nabla} J - (\vec{\nabla} J \cdot \vec{\nabla} L) \vec{\nabla} L \right] \tag{26}$$

where $\vec{\nabla} = \frac{\delta}{\delta b_i}$ and $\vec{\nabla} L = \frac{\vec{\nabla} L}{|\vec{\nabla} L|}$, an additional correction is applied as follows:

$$\delta\vec{b}_{corrected} = \delta\vec{b}_{projected} - \gamma \vec{\nabla} L \tag{27}$$

where $\gamma = \frac{L}{\vec{\nabla} L \cdot \vec{\nabla} L}$, and L is the difference between the current and the threshold value of the constraint function.

4 Verification of the hybrid CFD/FW-H solver

This section is focusing on the verification of the coupled CFD-CAA solver, given that the background CFD tool has adequately been validated in the past [13, 14].

4.1 Monopole in uniform flow

In the first case, results of the FW-H integral are compared to a well-known analytical solution of the sound field generated by a monopole source in a uniform flow. The stationary monopole source is located at the origin of the coordinate system and there is a uniform flow v_1 along the $+x$ direction. The complex velocity potential of the case is [19] :

$$\phi(\vec{x}_o, \vec{x}_s, \omega) = \frac{A i}{4\beta} \exp\left(i(\omega t + M_1 k \bar{x}_1)/\beta^2\right) H_0^{(2)}\left(\frac{k}{\beta^2}\sqrt{\bar{x}_1^2 + \beta^2 \bar{x}_2^2}\right) \tag{28}$$

where $\bar{x}_1$ and $\bar{x}_2$ are the same as in Eq. 6 and 7. The perturbation field of flow variables and variables needed to compute the F_i and Q in the FW-H integral are obtained from the real parts of $p' = \rho_0 \left(\frac{\partial \phi}{\partial t} + v_1 \frac{\partial \phi}{\partial x}\right)$, $u' = \nabla \phi$ and $\rho' = p'/c_0^2$. In this case, $M_1 = 0.6$, $A = 0.02\ m^2/s$ and $\omega = 0.162\ rad/s$. Fig. 3 compares the directivity plot at the radius of $R = 500m$ and fig. 4 shows the time history of p' at a receiver located at $(500m, 0m)$. The results of the FW-H integral exactly match the analytical solution. This is a convincing verification of the implementation of the 2D FW-H formulation, in problems with a uniform mean flow.

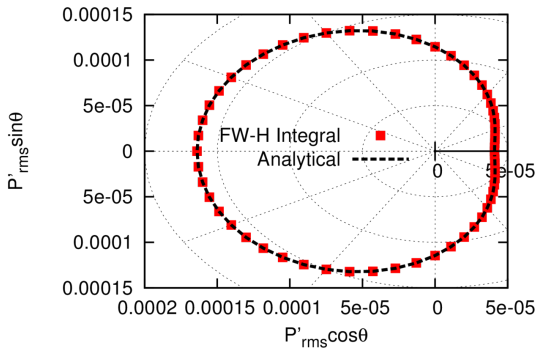

Fig. 3 Monopole source in uniform flow with $M_1 = 0.6$. Comparison of the directivity plots at $R = 500m$.

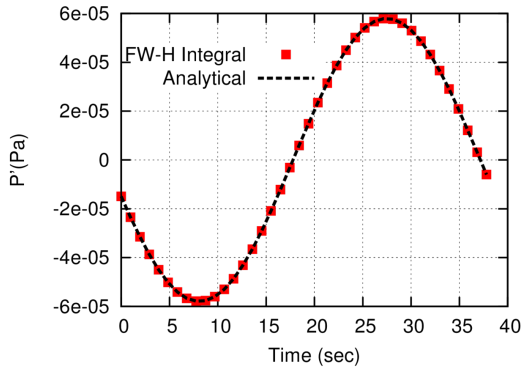

Fig. 4 Monopole source in uniform flow with $M_1 = 0.6$. Comparison of the time history of pressure fluctuation within a period, for a receiver located at $(500m, 0m)$.

4.2 Pitching airfoil in inviscid flow

In the second case, a comparison between the hybrid solver and the outcome of a pure CFD simulation is performed. A RAE2822 isolated airfoil is pitching about the quarter-chord point in an inviscid flow, with a 2 deg. amplitude and period equal to 0.114 sec. The free-stream Mach number is $M_1 = 0.6$ and the simulation computes 40 time steps per period. A 2D unstructured grid that extends 50 chords away from the airfoil is used, with 51000 nodes overall, among which 202 nodes on the airfoil contour and 151 nodes on the FW-H surface. The FW-H surface is placed at R=4C from the airfoil mid-chord (0.5C, 0), where C is the airfoil chord length. The directivity pattern at R=9C is plotted in fig. 5 and shows a very good agreement between results of the unsteady CFD (incl. post-processing of the computed pressure time-series along a circle with R=9C) and the application of the FW-H integral on the flow time-series computed along the FW-H surface.

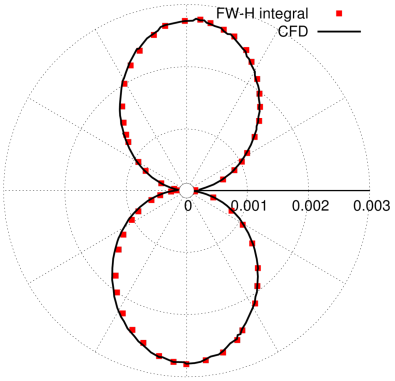

Fig. 5 Pitching isolated airfoil. Comparision of the directivity plots (p^0_{rms}° at radius R=9C.

5 Optimization results

Before proceeding to the aeroacoustic optimization, the computed gradients using the adjoint solver are verified w.r.t. those obtained by Finite Difference (FD) for the time-averaged lift force. The case and the computational grid are the same as the pitching RAE2822 isolated airfoil presented in section 4.2. The airfoil pressure and suction sides are parameterized using two Bezier curves, with 20 control points each, which are free to move in the y direction. Since the first and last control points are fixed, this case has 36 design variables. Figure 6 shows a good agreement between the gradients of the time-averaged lift force obtained by the two methods. Then, the so-computed adjoint sensitivities are used to run a shape optimization loop. Figure 7 shows the gradual increase in the lift force from its initial value after 7 optimization cycles, by changing the shape basically at the trailing edge, fig. 8.

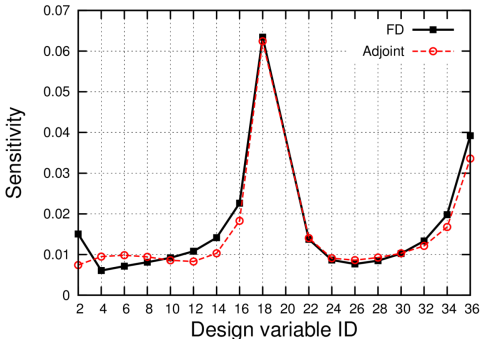

Fig. 6 Pitching isolated airfoil. Comparison of the time-averaged lift sensitivities for some control points, using the proposed adjoint method and FD.

Next, the optimization framework is used for aeroacoustic noise reduction. Starting geometry and flow conditions are the same as in the lift maximization problem, by minimizing the objective function of Eq. 8. In this case, a lift constraint is addi-

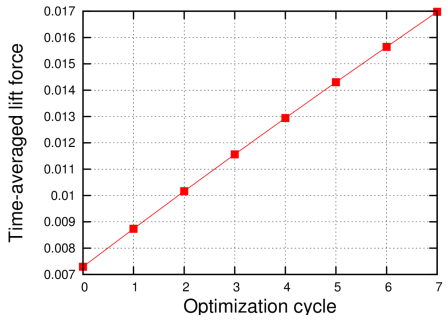

Fig. 7 Optimization of a pitching isolated airfoil (target lift). Evolution of the time-averaged lift force during the optimization loop.

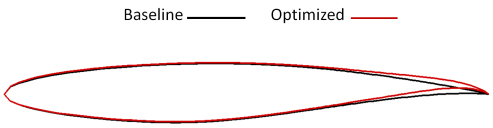

Fig. 8 Optimization of a pitching isolated airfoil (target lift). Shapes of the baseline and optimized airfoils.

tionally imposed using a gradient projection method based on a deferred correction scheme. The receiver is located at $\vec{x}_o = {}^1 0, \quad 20C^o$. To verify the computed gradients using the adjoint solver, these are compared with those obtained by FD in fig. 9. It shows a good agreement between the gradients obtained by the two methods. There are discrepancies at the trailing and leading edge areas; however, even for those control points, the gradients obtained by the two methods have the same signs.

Then, the adjoint-based shape optimization takes place. As illustrated in fig. 10, after 18 design cycles, the noise objective function, Eq. 8, is reduced by more than 60%. This figure also shows that the proposed constraint imposition method with the deferred correction keeps the time-averaged lift value almost constant, as it changes about 3% at the end. As expected, the reduction in the objective value results in a lower amplitude in pressure fluctuations, as shown in fig. 11. Figure 12 compares the directivity plot of the baseline and the optimized airfoils at the radius of R=20C and shows that the reduction in noise is omnidirectional. Figure 13 compares the baseline and the optimized airfoil shapes. It shows that the airfoil's shape is changed mainly close to the trailing edge while the rest of it remains almost intact. This practically reconfirms the important role of the airfoil trailing edge shape on noise generation.

6 Conclusions

The in-house flow/adjoint solver is extended to include an aeroacoustic noise prediction tool and its adjoint counterpart, based on the permeable version of the FW-H analogy in the frequency domain. The design sensitivities obtained by the continuous adjoint method are verified versus FD, for the noise objective function and the time-averaged lift for a pitching airfoil. Then, aerodynamic and aeroacoustic shape

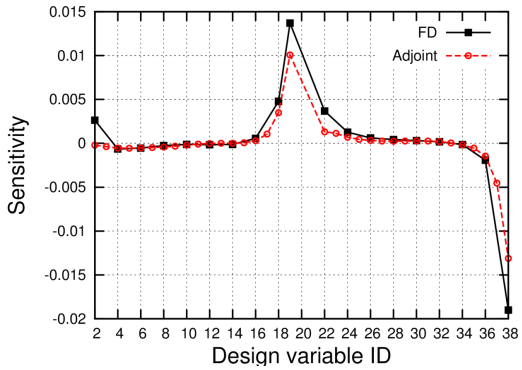

Fig. 9 Lift-constrained aeroacoustic optimization of a pitching isolated airfoil. Comparison of the noise (J as in Eq. 8) sensitivities for some control points, using the proposed adjoint method and FD.

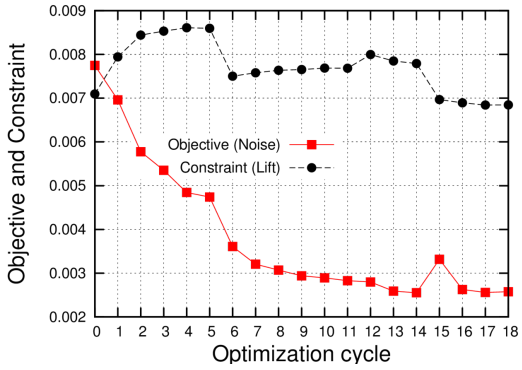

Fig. 10 Lift-constrained aeroacoustic optimization of a pitching isolated airfoil. Convergence of the objective and constraint functions.

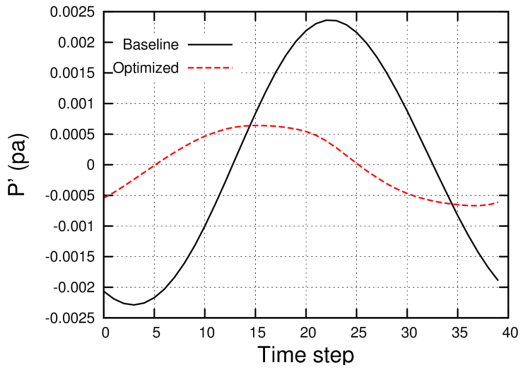

Fig. 11 Lift-constrained aeroacoustic optimization of a pitching isolated airfoil. Time history of pressure fluctuation within a period at the receiver's location.

optimization is performed and the results show that the objective values are significantly improved. The aeroacoustic optimization is subjected to an equality constraint on the lift. Results of the aeroacoustic optimization highlighted the importance of the trailing edge shape in airfoil self-noise generation.

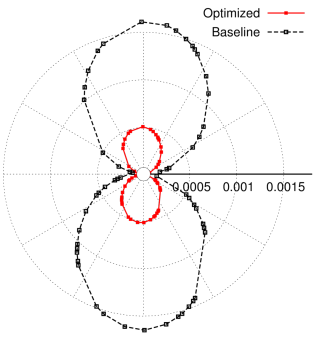

Fig. 12 Lift-constrained aeroacoustic optimization of a pitching isolated airfoil. Comparison of the directivity plots of the baseline and optimized airfoils at R=20C.

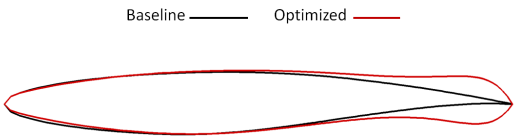

Fig. 13 Lift-constrained aeroacoustic optimization of a pitching isolated airfoil. Shapes of the baseline and optimized airfoils.

7 Acknowledgments

This project has received funding from the European Union's Horizon 2020 research and innovation program under the Marie Sklodowska Curie Grant Agreement No 722401.

References

1. Kallas, S., et al. : Flightpath 2050 Europe's vision for aviation. Report of the high level group on aviation research, European commission, Brussels, Belgium, Report No. EUR 98 (2011).
2. Pironneau, O. : On optimum design in fluid mechanics. Journal of Fluid Mechanics **64**(1), 97–110 (1974).
3. Jameson, A. : Aerodynamic design via control theory. Journal of scientific computing **3**(3), 233-260 (1988).
4. Papoutsis-Kiachagias, E. M. and Giannakoglou, K. C. : Continuous adjoint methods for turbulent flows, applied to shape and topology optimization: industrial applications. Archives of Computational Methods in Engineering **23**(2), 255–299 (2016).
5. Papoutsis-Kiachagias, E., Magoulas, N., Mueller, J., Othmer, C., and Giannakoglou, K. : Noise reduction in car aerodynamics using a surrogate objective function and the continuous adjoint method with wall functions. Computers & Fluids **122**, 223–232 (2015).
6. Rumpfkeil, M. and Zingg, D. : A hybrid algorithm for far-field noise minimization. Computers & Fluids **39**(9), 1516–1528 (2010).
7. Zhou, B., Albring, T., Gauger, N., Economon, T., Palacios, F., and Alonso, J. : A discrete adjoint framework for unsteady aerodynamic and aeroacoustic optimization. In 16th AIAA/ISSMO Multidisciplinary Analysis and Optimization Conference, 3355, (2015).

8. Zhou, B. Y., Albring, T. A., Gauger, N. R., Economon, T. D., and Alonso, J. J. : An efficient unsteady aerodynamic and aeroacoustic design framework using discrete adjoint. In 17th AIAA/ISSMO Multidisciplinary Analysis and Optimization Conference, 3369, (2016).
9. Zhou, B., Albring, T., Gauger, N., Ilario, C., Economon, T., and Alonso, J. : Reduction of airframe noise components using a discrete adjoint approach. In 18th AIAA/ISSMO Multidisciplinary Analysis and Optimization Conference, 3658, (2017).
10. Zhou, B. Y., Albring, T., Gauger, N. R., Ilario da Silva, C. R., Economon, T. D., and Alonso, J. J. : A discrete adjoint approach for jet-flap interaction noise reduction. In 58th AIAA/ASCE/AHS/ASC Structures, Structural Dynamics, and Materials Conference, 0130, (2017).
11. Economon, T., Palacios, F., and Alonso, J. : A coupled-adjoint method for aerodynamic and aeroacoustic optimization. In 12th AIAA Aviation Technology, Integration, and Operations (ATIO) Conference and 14th AIAA/ISSMO Multidisciplinary Analysis and Optimization Conference, 5598, (2012).
12. Kapellos, C. S., Papoutsis-Kiachagias, E. M., Giannakoglou, K. C.,and Hartmann, M. : The unsteady continuous adjoint method for minimizing flow-induced sound radiation. Journal of Computational Physics, **392**, 368–384, (2019).
13. Kampolis, I., Trompoukis, X., Asouti, V., and Giannakoglou, K. : CFD-based analysis and two-level aerodynamic optimization on graphics processing units. Computer Methods in Applied Mechanics and Engineering **199**(9-12), 712–722 (2010).
14. Asouti, V. G., Trompoukis, X. S., Kampolis, I. C., and Giannakoglou, K. C. : Unsteady cfd computations using vertex-centered finite volumes for unstructured grids on graphics processing units. International Journal for Numerical Methods in Fluids **67**(2), 232–246 (2011).
15. Yoo, C., Wang, Y., Trouve, A., and Im, H. : Characteristic boundary conditions for direct simulations of turbulent counterflow flames. Combustion Theory and Modelling **9**(4), 617–646 (2005).
16. Lighthill, M. J. : On sound generated aerodynamically ii. turbulence as a source of sound. Proceedings of the Royal Society of London. Series A. Mathematical and Physical Sciences **222**(1148), 1–32 (1954).
17. Curle, N. : The influence of solid boundaries upon aerodynamic sound. Proceedings of the Royal Society of London. Series A. Mathematical and Physical Sciences **231**(1187), 505–514 (1955).
18. Ffowcs Williams, J. and Hawkings, D. : Sound generation by turbulence and surfaces in arbitrary motion. Philosophical Transactions of the Royal Society of London. Series A, Mathematical and Physical Sciences **264**(1151), 321–342 (1969).
19. Lockard, D. : An efficient, two-dimensional implementation of the FfowcsWilliams and Hawkings equation. Journal of Sound and Vibration **229**(4), 897–911 (2000).